Vessel Wake Impact Forces on Marsh Scarps

Authors: Priestas, Anthony M., Styles, Richard, and Bain, Rachel

Source: Journal of Coastal Research, 39(2) : 207-220

Published By: Coastal Education and Research Foundation

URL: https://doi.org/10.2112/JCOASTRES-D-22-00056.1

Journal of Coastal Research	39	2	207–220	Charlotte, North Carolina	March 2023

Vessel Wake Impact Forces on Marsh Scarps

Anthony M. Priestas, Richard Styles*, and Rachel Bain

Coastal and Hydraulics Laboratory
U.S. Army Engineer Research and Development Center
Vicksburg, MS 39180, U.S.A.

www.cerf-jcr.org

www.JCRonline.org

ABSTRACT

Priestas, A.M.; Styles, R., and Bain, R., 2023. Vessel wake impact forces on marsh scarps. *Journal of Coastal Research,* 39(2), 207–220. Charlotte (North Carolina), ISSN 0749-0208.

A common morphological feature of high-energy coastal plain salt marshes is an erosive scarp separating the marsh platform from the abutting tidal flat. A noted deficiency in the understanding of scarp erosion is a lack of direct wave impact measurements to better constrain the physical processes driving material loss. To measure wave impact forces, load cells were embedded into a scarp face along the Intracoastal Waterway in northern Florida, which is frequented by shallow-draft vessels. The largest impact forces occurred when the mean water surface elevation was just below the midpoint of the scarp and decayed as the mean depth either increased or decreased. Early wave breaking around low tide reduced the direct impact on the scarp, whereas wave reflection around high tide reduced wave breaking and the associated maximum impact force. The sensitivity of impact force to tidal stage suggests that wave energetics (breaking *vs*. reflection) and scarp morphology (ramp *vs*. near-vertical surface) combine to produce a force pattern that favors maximum impact around midtide. Regression analysis indicated that the impact pressures were positively correlated with wave power and dynamic pressure, which are primary metrics used to model shoreline erosion. This study argues that the critical threshold for erosion may be refined by evaluating the relationship between impact pressures and marsh resistance, since wave exposure alone does not necessarily initiate erosion.

ADDITIONAL INDEX WORDS: *Erosion, salt-marsh retreat, wave breaking, intracoastal waterway, recreational watercraft.*

INTRODUCTION

Marsh edge erosion is a complex process primarily driven by mechanical energy transfer (*e.g*., wave attack), which acts to dislodge sediment, while biologically modulated soil properties act to resist erosive forces and regulate the rate of material loss. In high-energy environments, a common morphological feature is an erosive scarp separating the marsh platform from the abutting tidal flat (Allen, 1989, 2000). Observations and numerical models have shown that scarps can be nearly vertical and are self-sustaining even as the marsh edge recedes (Allen, 1989; Mariotti and Fagherazzi, 2010; van de Koppel *et al*., 2005; Van der Wal, Wielemaker-Van den Dool, and Herman, 2008). Because scarps are a common manifestation of eroding marsh boundaries, it is important to understand the physical processes that control the shape, stability, and persistence of these ubiquitous features. Lateral marsh erosion is likely the primary mechanism for marsh loss within estuaries and lagoons worldwide, as argued by Marani *et al*. (2011), especially in the absence of sediment supply, leading to the concept that marsh boundaries are inherently unstable features (Fagherazzi *et al*., 2020; Mariotti and Fagherazzi, 2020).

The primary assailing forces can be generated by wind waves or vessel wakes. Erosion due to wind wave attack has been studied extensively using empirical and numerical models. Although Schwimmer (2001) found a slight power-law relationship (exponent of 1.1) between erosion rates and incident wave power, subsequent studies empirically described the relationship as linear but with a high degree of scatter (Leonardi *et al*., 2016; Marani *et al*., 2011; Mariotti and Fagherazzi, 2010; McLoughlin *et al*., 2015; Priestas *et al*., 2015). This relationship is often used to describe the driver of marsh retreat in numerical model investigations (Bendoni *et al*., 2019; Mariotti and Carr, 2014; Mariotti and Fagherazzi, 2010; Valentine and Mariotti, 2019).

Compared to wind waves, the contribution of vessel wakes to edge erosion is poorly constrained. At marshes adjacent to open water, the fraction of total wave energy from vessel wakes is small and thus expected to contribute little to erosion rates. However, vessel wakes within interior waterways are often suspected to be the primary cause of erosion in these settings. Consequently, vessel-generated waves have been studied in the context of wetland impacts in regions with limited fetch or along active navigation corridors (Bilkovic *et al*., 2017, 2019; Houser, 2010; Safak, Angelini, and Sheremet, 2021; Safak *et al*., 2020). Additionally, large commercial vessels such as cargo ships and tankers can produce 0.5 to 1.0 m fluctuations in water level that have been implicated as a cause of wetland erosion near deep-draft navigation channels (Herbich and Schiller, 1985; Maynord, 2003, 2007; Rapaglia *et al*., 2011).

In interior regions, where wetlands are sheltered from wind waves and large wakes associated with commercial ships, recreational vessels are the major sources of wave energy (Maynord, 2003, 2005; Safak, Angelini, and Sheremet, 2021; Shuster *et al*., 2020; Styles and Hartman, 2019) and continue to be a source of public concern, resulting in calls for increased restrictions or regulations (Bilkovic *et al*., 2017). Although

DOI: 10.2112/JCOASTRES-D-22-00056.1 received 24 June 2022; accepted in revision 24 October 2022; corrected proofs received 14 December 2022; published pre-print online 20 January 2023.
*Corresponding author: richard.styles@usace.army.mil

recreational vessels typically do not generate waves as large as commercial vessels, they can travel at high speeds closer to the shoreline and thus directly impact shorelines of wetland interiors. In one example, Houser (2010) found that although recreational vessels represented only a small fraction of the total wave energy, they accounted for 25% of the total wave force, as calculated from Hughes' (2004a, 2004b) wave momentum flux parameter. Field studies by Silliman *et al*. (2019) highlighted the potential for vessel wakes to cause vegetation dieback and subsequent marsh degradation. Vessel wakes near the shoreline can also enhance localized sediment resuspension and transport. For example, field data from Safak, Angelini, and Sheremet (2021), taken along the Atlantic Intracoastal Waterway near St. Augustine, Florida, showed increased sediment concentrations by an order of magnitude and a 12% increase in sediment transport in the presence of vessel wakes. Considering that recreational vessel use is rising globally (Burgin and Hardiman, 2011; Carreño and Lloret, 2021), coastal plain salt marshes will be affected by an increase in the number of small craft and greater erosion potential and sediment transport along sheltered marsh perimeters.

The energy density of vessel-generated waves is regulated by vessel traffic patterns, which are generally highest during daylight hours and on weekends and holidays (Buckingham *et al*., 1999). Recreational boating activities can also vary by season, such that the energy flux is highly variable and difficult to quantify over erosional timescales (Bilkovic *et al*., 2019). The disparity between erosional and vessel monitoring timescales, combined with the fact that the present understanding of the physical relationship between wave power and marsh retreat is far from comprehensive (Bloemendaal *et al*., 2021; Finotello *et al*., 2020), makes it difficult to develop energy-based vessel wake erosion models. Therefore, the purpose of this study was to quantify vessel-generated impact forces along a scarped, cohesive shoreline and to develop a first-order transfer function relating vessel wave dynamics to those forces. This approach is considered to be a significant step in advancing the present knowledge of vessel-induced marsh edge erosion because the direct impact forces are quantified on the timescales of vessel wake action. As marsh creation projects are increasingly utilizing nature-based solutions, such as beneficial use of dredged material and living shorelines (Bridges *et al*., 2015; Safak *et al*., 2020), it will be important to understand the relationship between wave energy and wave forcing to predict the performance and life cycle of these engineered solutions.

For this research, sensors for measuring impact forces and vessel wake characteristics were deployed at an eroding marsh edge along the Intracoastal Waterway (IWW) in St. Johns County, Florida. This segment of the IWW is fetch-limited and receives high volumes of recreational traffic, such that most impact forces are from vessel wakes (Safak, Angelini, and Sheremet, 2021). The following sections describe the study site, the instrumentation, the data processing, and the vessel wake analysis. Because load cells have not previously been used for measuring scarp impact forces, attention is given to the deployment setup and data processing techniques. Results describe the vessel characteristics, the wave characteristics (height, period, energy flux, total energy, and dynamic pressure), and the vertical variation in the shore-normal wave forces. Statistical relationships between impact forces and the derived wave quantities are presented. The discussion focuses on the implications of the tide-dependent vertical distribution of impact pressure for marsh edge erosion and on the relationship between the normal forces and the offshore vessel wake characteristics. This study also evaluated the implications of utilizing impact forces to define erosion thresholds, which are currently not well constrained, in future studies.

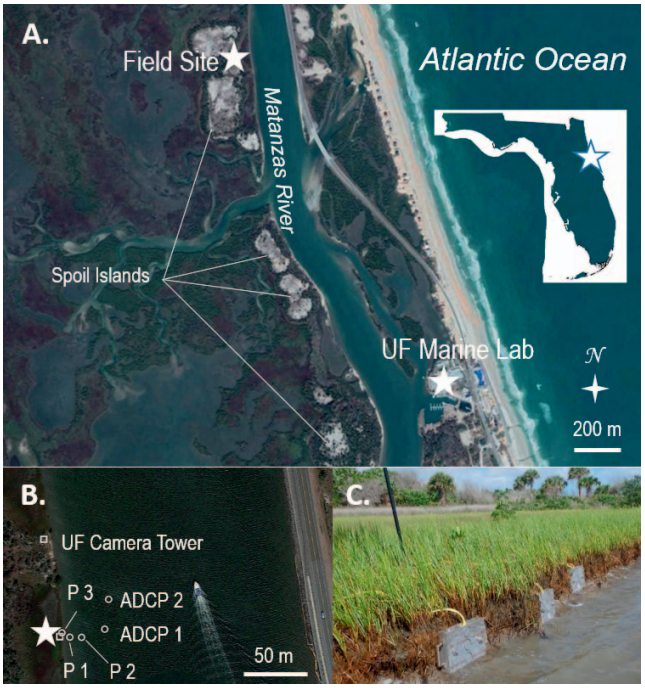

Figure 1. Location map of the study area along the IWW in northern Florida (A), with instrument locations (B), and configuration of the load cell arrays (C). ADCP1 was configured to measure waves only. Paros pressure sensors P1 and P2 were deployed offshore to measure wave attenuation, while P3 was installed on the marsh platform to capture wave propagation during high water levels.

METHODS

The field experiment was conducted along the IWW within the Matanzas River estuary in St. Johns County, Florida (29.68177°N, 81.22414°W), which cuts through back-barrier and fringing marshlands of the Guana Tolomata Matanzas (GTM) Research Reserve (Figure 1). The location was selected due to the presence of an actively eroding scarp and the relatively high instances of vessel traffic (Safak, Angelini, and Sheremet, 2021). Channel margins of the IWW consist of salt marsh, dredge spoil islands, uplands, and intertidal mud flats and shoals. Elevated shoreline margins will often have a scarped morphology, which is indicative of an erosive feature. At the study site, the marsh scarp height was approximately 0.40 m. Soil characteristics were not quantified, but previous coring work in the area revealed an average sediment composition of 20% sand, 77% silt, and 3% clay, with 10% organics (Silliman *et al*., 2019). The absence of large, detached sections of marsh suggests that material loss is primarily

through abrasion or surface erosion as opposed to block failure. The tidal regime is semidiurnal with mean neap and spring tide ranges of approximately 1.0–1.8 m near the Matanzas Inlet (Gallivan and Davis, 1981), though they appear to be somewhat damped near the study site (0.6–0.9 m) based on the water-level measurements.

Wave Impact Forces

Horizontal impact forces were measured using a vertical array of submersible, S-type strain gauge load cells (model HRS-1K, Load Cell Central, Inc.). The full-scale output of the load cells is 2 mV/V of excitation, and they provide a highly linear response. The capacity of each load cell is 4448 N in compression and tension. Nonlinearity in the output is reported as 0.1% of full scale by the manufacturer; thus, the load cells are capable of resolving 2.2 N in tension or compression with a high degree of confidence. The load cell data were collected at approximately 3200 Hz; sampling frequencies greater than 2000 Hz are necessary to prevent significant reductions in peak force and pressure measurements due to the fast rise times of impact loads (Schmidt, Oumeraci, and Partenscky, 1992).

A schematic drawing of a load cell array is shown in Figure 2. These were designed to be modular to accommodate various scarp heights, and each panel of the array could accommodate three load cells. The load cells were firmly secured to the rear mounting plate on one end, while the other end remained freestanding within a circular cutout of slightly larger diameter. A face plate was affixed to the front of each load cell to increase the forces. The face plate diameter was considered to be large enough to register adequately small compressive forces from vessel wakes, yet small enough to avoid torque from off-axis loading. When assembled, the load plates were flush with the front panels. The arrays were firmly secured to the face of the scarp using two 0.7 m screw Earth anchors per array, as any play between the array and scarp could dampen wave forces.

Waves and Hydrodynamics

A schematic diagram of the instrument deployment is shown in Figure 3. The instrument array consisted of two Nortek Signature1000 acoustic Doppler current profilers (ADCPs; ADCP1 and ADCP2) and three Paros (Series 8DP) Digiquartz pressure sensors (P1, P2, and P3) collocated in a shore-perpendicular transect.

The ADCPs were deployed approximately 35 m from the left-descending shoreline in 3.0–3.5 m of water. The first ADCP (ADCP1) was dedicated to measure waves using 8 Hz acoustic surface tracking with the burst interval set to 3600 s (essentially continuously); however, it was discovered that the instrument failed to record accurate wave heights. Consequently, only the pressure data from ADCP1 were used to resolve the tidal signal. Paros sensor P1 was mounted with the transducer located approximately 0.25 m above the bed, with an elevation relative to the marsh platform of –0.8 m.

Load Cell Arrays

Three load cell arrays (A1, A2, A3) were mounted vertically into the face of the scarped shoreline, spaced approximately 1 m apart. Since the marsh scarp height was 0.38–0.40 m, only one panel was needed for each array. From this configuration, the spatial variability of forces along the vertical and horizontal dimensions of the scarp could be investigated.

Vessel Characterization

Vessel passage events were captured using a Mobotix M16 camera with motion detection capabilities. Vessel passages were recorded as still images within a predetermined image window set inside the camera's field of view. The image window was constrained to the IWW channel margins to limit false detections. The event dead time, meaning the minimum time required to reset the camera after an image capture, was set to 5 seconds. During periods of high vessel traffic, multiple vessels were captured in a single image. Consequently, individual vessels and their wakes could not be uniquely identified in the wave record in these instances. The research vessel (RV) *Parker*, operated by the research team, was also used to generate wakes to increase the number of vessel wake measurements available for analysis. The RV *Parker* is a 7 m (23 ft) cabin vessel with a V-shaped hull, 38 cm (15 in.) draft, and twin 200 hp outboard motors. The team used the RV *Parker* to simulate different modes of operation scenarios amongst recreational vessels, such as planing and semiplaning speeds and distance from the shoreline.

Data Acquisition

Two separate data acquisition (DAQ) systems were used, one to collect data from the load cells and one to collect data from the Paros sensors and camera. Power was supplied to the systems using 12 V AGM batteries and a solar panel with charge controller to maintain voltage. The DAQ systems ran independently of each other, while the ADCP data were stored internally, which made time synchronization of the data challenging. However, these issues were handled in postprocessing and are explained further in the next sections. A real-time telemetry unit (RTU) handled data acquisition processes, storage, and wireless transmission of data. Time stamps of all data streams were stored in Coordinated Universal Time (UTC). Data telemetry was supplied *via* cellular modem and transmitted once per day to a local server.

Load Cell Postprocessing

The conversion from load cell counts to force was based on static laboratory tests. Lead ingots of known weight were stacked sequentially on each load cell at 20 N increments to determine the response to compressive forces ranging between 0.8 N (the weight of the face plate alone) and 423 N. The relationship between counts and force was found to be highly linear over the tested range, with a best-fit conversion factor of 6.5×10^{-2} N per count. Moreover, the response to a given force was approximately symmetric during loading and unloading. After subtracting the weight of the face plate, the load cells should record a value of zero in still water because the water pressure on the front of the face plate is balanced by water pressure on the back of the face plate. However, several of the field data sets were offset from zero and/or displayed a nonlinear drift over the recording duration (Figure 4a). This may have been due to diurnal temperature variations. All offsets from zero mean load were corrected by subtracting a 2 minute windowed average from the measured values.

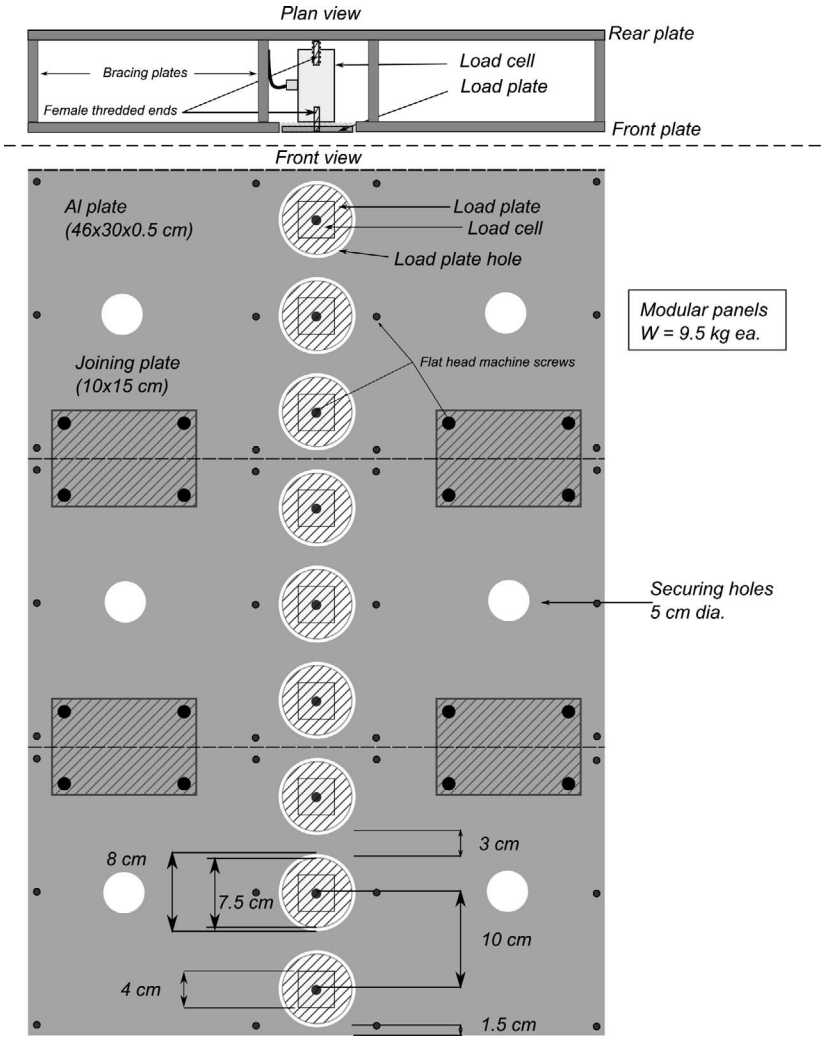

Figure 2. Schematic diagram of modular load cell array shown in plan view (above) and side view (below).

Some of the field-collected load cell data contained a small-amplitude 16 Hz oscillation, which was interpreted as electrical interference from the Paros instruments. A wavelet denoising routine was implemented to remove the high-frequency noise after preliminary experimentation indicated that a fast Fourier transform (FFT) denoising algorithm would alter the shape of wake-generated compressive impulses. The signal was decomposed to 16 levels using a discrete stationary wavelet transform with the Symlets 2 (sym2) wavelet. Thresholds were then applied to the wavelet coefficients to remove low-amplitude, high-frequency oscillations while retaining high-amplitude, high-frequency energy during wake impacts on the load cell. Importantly, this algorithm preserved the signal shape and magnitude while removing the electrical noise (Figure 4b,c).

Pressure Sensor and ADCP Postprocessing

Although the Paros pressure sensors were programmed for 16 Hz sampling, the output sampling rate was determined to be irregular during postprocessing (Figure 5a,b), with instantaneous sampling rates ranging between 1 Hz and 31 Hz. It was therefore necessary to linearly interpolate onto an even abscissa before proceeding with spectral analysis of the data sets. However, no interpolation was performed if the instantaneous sampling rate dropped below 4 Hz to ensure adequate data for characterizing small-period wakes. Measurements separated by a time step $\Delta t > 0.25$ seconds were flagged as "no data," and all wake events containing one or more "no data" values were discarded from further analysis (Figure 5c,d). Following interpolation, the pressure data were converted to depth of water column using an FFT-based dynamic pressure correction from the OCEANLYZ Matlab toolbox (Karimpour, 2020; Karimpour and Chen, 2017). Because tidal stage variations caused attenuation at the sensor to vary through time, the algorithm was applied to 10 minute windows of data centered on each individual wake event.

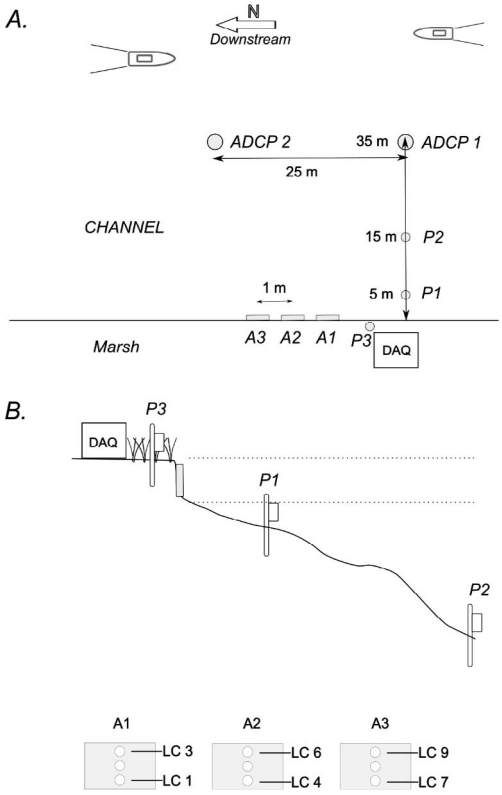

Figure 3. Plan view (A) and cross-section view (B) of the instrument deployment and their relative positions. Waves were measured at ADCP1 and Paros sensors P1–P3. ADCP2 measured current profiles.

Vessel Detection Postprocessing

The image data set from the Mobotix camera was first reduced by visual inspection to eliminate false detections. The vessel images were used to build a timetable of passage events and to classify the events by vessel type and wake size. The utility ExifTool (www.exiftool.org) was used to extract image capture dates and times from the metadata files. Parameters and their classification codes and meanings are provided in Table 1. (Note: The classification efforts are to a degree subjective and may not reflect the true distributions.) During times of heavy vessel traffic, it was not uncommon to have multiple vessels within the same image capture.

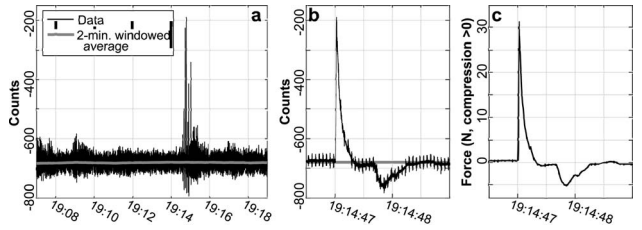

Figure 4. Example of load cell postprocessing. Time stamps are HH:MM or HH:MM:SS, UTC. (a) Twelve minutes of raw load cell data overlaid with 2 minute windowed average. Note the substantial offset from zero mean load. (b) Detail of subplot (a) with 16 Hz noise visible. The horizontal axis spans 2.5 seconds. (c) Detrended and wavelet-denoised data converted from counts to force in Newtons. Compressive forces are positive, and tension forces are negative.The wavelet denoising preserves the shape of the wake impact signal while removing the low-amplitude, high-frequency electrical noise.

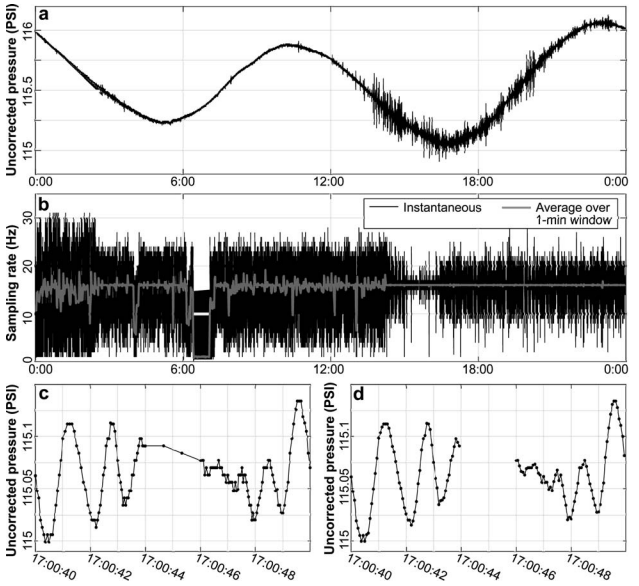

Figure 5. (a) Paros pressure sensor data collected in St. Augustine on 26 September 2020. Time stamps are HH:MM or HH:MM:SS, UTC. (b) Sampling rate for the time series in subplot (a). Although the instruments were programmed for constant 16 Hz sampling, the actual instantaneous sampling rate varied between 1 Hz and 31 Hz. (c) Detail of subplot (a) with the horizontal axis spanning 10 seconds. Note the variable sampling rate, which is particularly evident between time stamps 17:00:44 and 17:00:46. (d) During postprocessing, the data were linearly interpolated onto an even 16 Hz abscissa to permit spectral analysis. However, because the vessels of interest produced wake periods as small as $T = 1$ s, linear interpolation was inappropriate when the sampling rate was excessively low. Any measurements separated by more than 0.25 seconds in subplot (c) were consequently marked as "no data" and were discarded from further analysis.

Wake Event Characterization

Wake events were interactively identified in a graphical interface by overlaying the pressure time series and the known time stamps of vessel passages derived from the motion-sensing camera. Because the instruments' internal clocks were not synchronized, the start time t_{start} of each wake event was placed at a time preceding the arrival of wake energy at any instrument, and the end time t_{end} was placed at a time after wake energy had dissipated at all instruments. If the start time stamp of a given wake event occurred before the end time stamp of the previous events, these were merged into a single "multivessel" event during subsequent calculations.

After establishing the start and end times of each wake, wake characteristics were calculated for each event. Individual half-oscillations (*i.e.* crests and troughs) with a minimum amplitude of 0.05 m were identified based on crossings of the mean depth

Table 1. *Parameters and codes used in the vessel classification analysis.*

Parameter	Classifications
Vessel type	BWG (barge)
	BWR (bow rider/deck boat)
	CTR (center console)
	DNG (dingy)
	JET (jet ski)
	PON (pontoon)
	PWR (power boat)
	SLB (sailboat)
	SDB (sedan bridge)
	SKF (skiff)
	TWR (trawler)
	TUG (tugboat)
	YHT (yacht)
	PKR† (R/V Parker, US Army Corps of Engineers)
On plane	1 (Yes), 2 (No)
Direction	N (north), S (south)
Class	A (<4.5m) (<16 ft)
	1 (4.5–8.0m) (16–26 ft)
	2 (8.0–12.0m) (27–40 ft)
	3 (>12m) (>40 ft)
Channel location	RD (right descending third)
	LD (left descending third)
	CTR (center third)
Wake size	S (small)
	M (moderate)
	L (large)
	N (none)

†*Vessel type PKR indicates the research vessel Parker, which was used to generate wakes during times of low vessel traffic. PKR images were pulled from the characterization analysis to better reflect typical vessel conditions during the deployment period. The wake signature from PKR was included in the wake analysis, however.*

d between t_{start} and t_{end}. The wave height H_i for the ith half-oscillation was then calculated as twice the vertical distance between d and the ith extreme value (Figure 6a). The peak wake period T_p was assigned based on the wavelet transform of the surface elevation time series (Figure 6b).

Energy Flux and Dynamic Pressure Calculations

The energy flux corresponding to the ith half-oscillation was calculated as:

$$(E_f)_i = \frac{\pi}{8T_p k}\rho g H_i^2\left(1+\frac{2kd}{\sinh(2kd)}\right)\left[\frac{\mathrm{M}\cdot\mathrm{L}}{\mathrm{T}^3}\right] \quad (1)$$

where, ρ is the water density, g is the gravitational acceleration, and k is the wavenumber determined from the dispersion equation:

$$\left(\frac{2\pi}{T_p}\right)^2 = gk\tanh(kd) \quad (2)$$

Multiplying Equation (1) by $T_p(\rho g)^{-1}d^{-3}$ gives the normalized energy flux:

$$\left(E_f^*\right)_i = \frac{\pi}{8kd}\left(\frac{H_i}{d}\right)^2\left(1+\frac{2kd}{\sinh(2kd)}\right)[-] \quad (3)$$

In the subsequent analysis and discussion, only the maximum value of $\left(E_f^*\right)_i$, which corresponds to the maximum value of H_i, is retained.

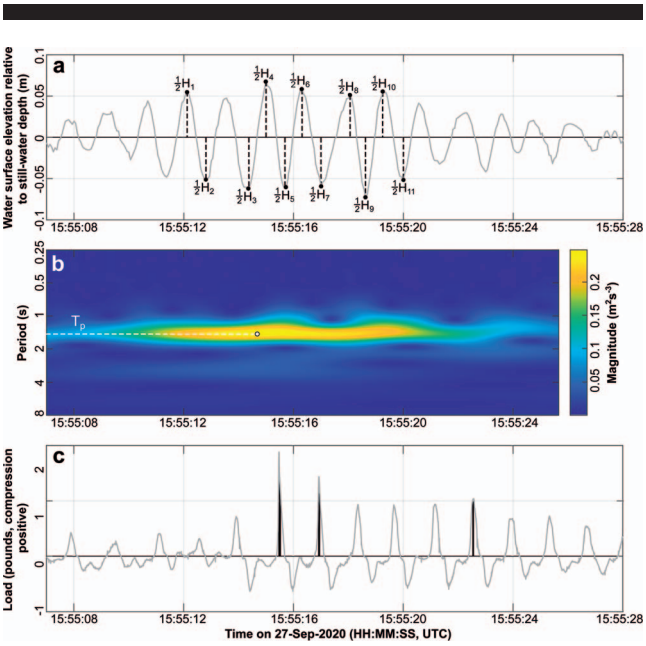

Figure 6. Definition of variables, including (a) the wake amplitude H_i, which was defined as twice the amplitude of the ith half-oscillation exceeding a 5 cm threshold, and (b) the peak wake period T_p, which was determined from the wavelet transform. The impulse on the marsh scarp was defined as the time integral of all instantaneous load values exceeding 1 pound (0.45 kg), which is illustrated by the black shaded area in subplot (c). Note that all time stamps are formatted as HH:MM:SS.

The total energy for a wake event containing N half-oscillations was calculated as:

$$E_{tot} = \frac{1}{2}T_p\sum_{i=1}^{N}(E_f)_i$$

$$= \frac{\pi\rho g}{16k}\left(1+\frac{2kd}{\sinh(2kd)}\right)\sum_{i=1}^{N}H_i^2\left[\frac{\mathrm{M}\cdot\mathrm{L}}{\mathrm{T}^2}\right] \quad (4)$$

or nondimensionally as:

$$E_{tot}^* = \frac{\pi}{16kd}\left(1+\frac{2kd}{\sinh(2kd)}\right)\sum_{i=1}^{N}\left(\frac{H_i}{d}\right)^2[-] \quad (5)$$

Note that the factor of ½ in Equation (4) accounts for the measurement of H_i at both the crest and the trough, which results in a double-counting of each full-phase oscillation.

The linearized maximum dynamic pressure under a wave is written as:

$$(P_{d,av})_i = \rho g\frac{H_i}{2}\frac{\cosh k(d+z)}{\cosh kd}\left[\frac{\mathrm{M}\cdot\mathrm{L}}{\mathrm{T}^2}\right] \quad (6)$$

where, z is the vertical coordinate measured positive upwards from the still-water level. Vertically integrating and then dividing by $\rho g d^2$ yields the depth-integrated dynamic pressure in nondimensional form:

$$\left(P^*_{d,av}\right)_i = \frac{H_i}{2kd^2}\frac{\sinh(kd)}{\cosh(kd)}[-] \quad (7)$$

For each wake event, only the maximum value of $\left(P^*_{d,av}\right)_i$ was retained; this maximum is labeled $P^*_{d,av}$ in subsequent analyses and discussion.

Load Cell Force Calculation

The force on each load cell was measured over the area of the circular face plate, $A_{\text{plate}} = 0.0046\ \text{m}^2$. For clarity, this force is denoted $(F^{FP})_j$, where j is the index of the load cell. To standardize comparison with earlier research, force was converted to a spatially averaged, time-maximum impact pressure for each wake event:

$$P_{max} = \frac{1}{M \cdot A_{plate}} \sum_{j=1}^{M} \left(F^{FP}_{max}\right)_j \left[\frac{\text{M} \cdot \text{L}}{\text{T}^2}\right] \quad (8)$$

where, $\left(F^{FP}_{max}\right)_j$ is the maximum force recorded by the jth load cell during the wake event, and M is the total number of load cells. Equation (8) may be normalized by the hydrostatic pressure as:

$$P^*_{max} = \frac{P_{max}}{\rho g d}[-] \quad (9)$$

Before calculating the compressive impulse, all instantaneous forces below a threshold of 4.45 N (1 pound) were set to zero:

$$F^{FP}_{c,j}(t) = \begin{cases} 0, F^{FP}_j(t) < 4.45N \\ F^{FP}_j(t), F^{FP}_j(t) \geq 4.45N \end{cases} \quad (10)$$

The spatially averaged compressive impulse was then defined as:

$$I = \frac{1}{M \cdot A_{plate}} \sum_{j=1}^{M} \left[\int_{t_{start}}^{t_{end}} F^{FP}_{c,j}(t)\text{d}t\right] \left[\frac{\text{M}}{\text{L} \cdot \text{T}}\right] \quad (11)$$

The application of Equation (10) was necessary to account for imperfect instrument synchronization, which often resulted in a nonnegligible duration of time between t_{start} and the arrival of wake energy at the load cells. If Equation (10) had not been applied, then small oscillatory forces on the scarp preceding the arrival of the wake would have been included in the time integral represented by Equation (11), artificially increasing the calculated value of I. A graphical representation of the integral in Equation (11) appears in Figure 6c. Equation (11) can be normalized as:

$$I^* = \frac{I}{\rho g d T_p}[-] \quad (12)$$

RESULTS

The data set is summarized in Figure 7. Due to high volumes of vessel traffic during some of the recording time, significant overlap in the arriving wake of multiple vessels ("MULTI", Figure 7a) made it difficult to identify individual vessel wake signatures. This resulted in several long-duration wake events containing up to 40 full-period oscillations exceeding the amplitude threshold of $H > 0.1$ m at Paros 1 (Figure 7b). However, dividing the number of oscillations by the number of vessels passing during the event suggests that the average number of oscillations per vessel rarely exceeded 15 (Figure 7c). The average value of T_{p} at Paros 1 was 2.2 seconds with a maximum of 4.9 seconds, while the maximum wake height H was 0.49 m (Figure 7d,e). The maximum depth-normalized wave height was $H/d = 0.82$ at Paros 1, with smaller values being more common (Figure 7f). The distributions of peak energy flux and total energy at Paros 1 (Figure 7g,h,i), along with the maximum impact pressure and total compressive impulse at the load cells (Figure 7j,k,l), were strongly right-skewed.

Figure 8 displays the average value of peak energy flux for all vessels within a given class. The RV *Parker* ("PKR") generated the largest peak energy flux, on average, although this value is atypically large due to the intentional creation of large wakes for research purposes. For vessels under typical operation, the largest peak energy fluxes correspond to class trawler (TRW).

Effect of Tidal Stage on Impact Pressure

Figure 9 displays the variation in impact pressure with both water depth and measurement elevation. The water depth has been normalized as:

$$d^* = \frac{d_{scarp} - z_{base}}{z_{top} - z_{base}} \quad (13)$$

where, z_{base} is the elevation of the scarp toe, z_{top} is the elevation of the marsh, and d_{scarp} is water depth at the toe of the scarp (*i.e.* depth above z_{base}). Consequently, $d^* = 0$ when the water level is at the base of the scarp, and $d^* = 1$ when the water level is even with the marsh platform. In Figure 9a,b,c, the measurement elevation is fixed at a specific point on the marsh scarp, while the water level varied due to the tide. The largest impact pressures, which approach 10 kPa in the 99th percentile of data, occurred when the mean water surface elevation was just below the midpoint of the scarp and decayed to <1 kPa as the mean depth approached either the top or toe of the marsh scarp.

The horizontal variability in measured force is shown in Figure 9d,e. Figure 9d displays the average impact pressure on panel 1 (*i.e.* average of measured peaks from load cells 1, 2, and 3), while Figure 9e displays the same measurement for panel 2 (load cells 4, 5, and 6). Note that panel 3 is not included in Figure 9 due to irregularities in the performance of load cell 9. There is nonnegligible horizontal variability in the measurements. For example, panel 2 recorded a maximum impact of 8.7 kPa, whereas panel 1 recorded a smaller maximum impact of 6.2 kPa. Despite the variation in magnitude, the results from the two panels are qualitatively similar in the sense that maximum impact forces occurred when the water level was slightly below the middle of the scarp.

The relationship between water depth and peak force displayed in Figure 9a–e does not appear to be attributable to variations in wake height at different tidal stages. Figure 9f displays the distribution of peak wake heights for all wake events within depth bins spanning 25% of the total scarp height. The median value of the peak wake heights

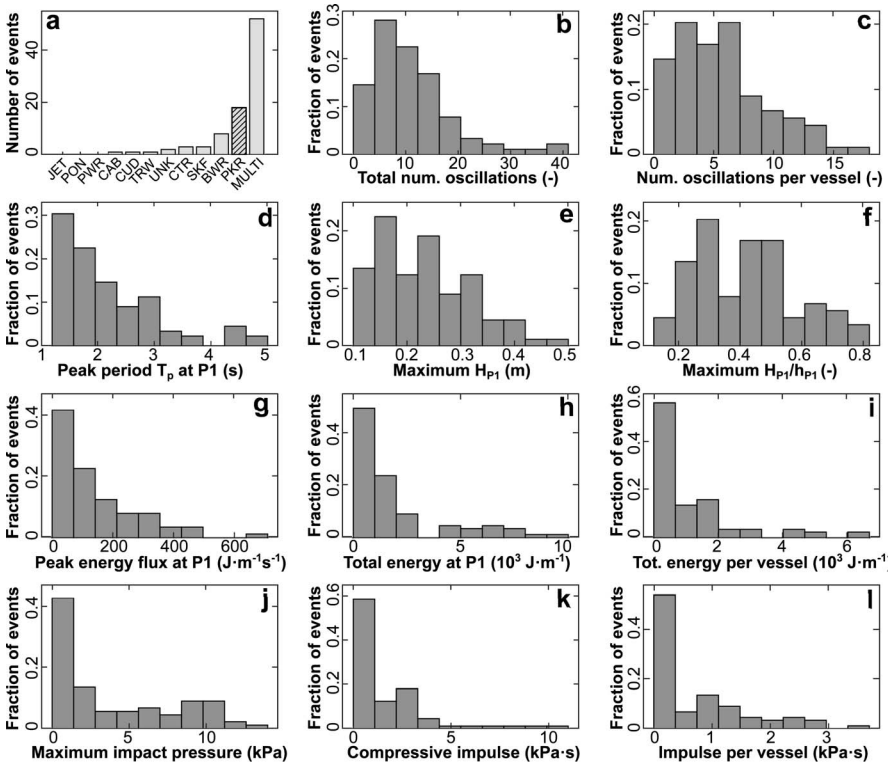

Figure 7. Summary of wake event characteristics. (a) Count of events for each vessel class. The "MULTI" category corresponds to events with multiple vessels that could not be separated into individual wakes. (b) Number of full-period oscillations with height $H > 0.1$ m at Paros 1 during each wake event. (c) Same as b, but the count has been normalized by the number of vessels passing during the wake event. (d) Peak wake period at Paros 1 during each wake event. (e) Maximum wake height at Paros 1 during each wake event. (f) Maximum depth-normalized wake height at Paros 1. (g) Maximum energy flux at Paros 1. (h) Total wake energy at Paros 1. (i) Same as h, but the total energy has been normalized by the number of vessels passing during the wake event. (j) Maximum impact pressure at the scarp during each wake event. (k) Total compressive impulse at the scarp during each wake event. (l) Same as k, but the impulse has been normalized by the number of vessels passing during the wake event.

systematically increased with increasing water depth until the tide exceeded 75% of the scarp height. Moreover, the absolute maximum wake height of 0.49 m occurred when the water depth was only 0.03 m below the top of the scarp. These results indicate that the relatively larger impact forces for water levels below the scarp midpoint were not due to larger wake heights at low water, but rather due to some depth-related changes in the ways in which the wakes interact with the scarp.

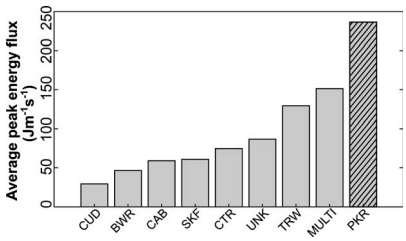

Figure 8. Average of peak energy flux for each vessel class.

It should likewise be noted that the largest wakes did not always generate the largest impact forces on the scarp. For each depth bin, Figure 9f also displays the height of the wake generating the largest impact on the upper (green × symbol), middle (blue ○), and lower (red •) segments of the scarp. When the tide was above the midelevation of the scarp, the largest impacts at all elevations on the scarp were generated by wakes with a height between 0.35 and 0.40 m. However, for lower tidal stages, the largest impacts were often generated by smaller-height wakes, particularly at the midelevation of the scarp (blue × in Figure 9f). For the lowest water level bin, the largest impact on the uppermost load cell was generated by the smallest wake height.

Relationship between Energy Flux and Impact Pressure

The relationship between the maximum nondimensional energy flux, E_f^* at Paros 1, which is the maximum value of $\left(E_f^*\right)_i$ given by Equation (3), and the maximum nondimensional impact pressure on the scarp, P_{max}^*, given by Equation (9), is shown in Figure 10a–c. The sensitivity of maximum impact pressures to tidal elevation (Figure 9) suggests the existence of different forcing regimes—one for the high-impact area on the lower half of the scarp and a second for the lower impact area on

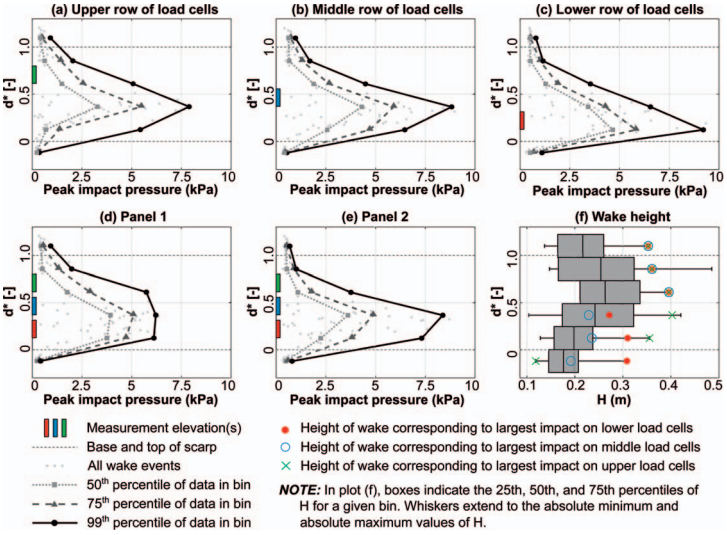

Figure 9. Variation in peak impact pressure with water depth for (a) the upper row of load cells, (b) the middle row of load cells, (c) the lower row of load cells, (d) panel A1, and (e) panel A2. For each 0.10 m depth bin, subplot (f) displays the distribution of peak wake heights within that bin. The height of the wake generating the largest impact on each row of load cells is indicated by the colored symbols; note that the largest wakes did not always generate the greatest impacts.

the upper half of the scarp. Accordingly, the scarp was partitioned into lower ($0 < d^* < 0.5$) and upper ($0.5 < d^* < 1$) domains, where d^* is the nondimensional water depth at the scarp as defined in Equation (13). Because all waves with $H < 0.1$ m were excluded, impacts in the region $d^* < 0.25$ are due primarily to runup, which means the force mechanism is not caused by direct impact on the scarp. As such, the scarp was further partitioned for $d^* < 0.25$. For comparison, the relationship between impact forces and wave characteristics without partitioning is also presented in Figure 10d. Using linear least squares on the log-transformed data, the best-fit relationships between the nondimensional maximum impact pressure and nondimensional maximum energy flux were found to be:

$$P^*_{max} = 2.20\left(E^*_f\right)^{0.25} \quad (0 \le d^* < 0.25)$$

$$P^*_{max} = 4.10\left(E^*_f\right)^{0.64} \quad (0.25 \le d^* < 0.5)$$

$$P^*_{max} = 1.14\left(E^*_f\right)^{0.41} \quad (0.5 \le d^* \le 1)$$

$$P^*_{max} = 2.76\left(E^*_f\right)^{0.53} \quad (0 \le d^* \le 1) \qquad (14)$$

with R^2 values of 0.22, 0.73, 0.72, and 0.50, respectively (Figure 10a–d). Note that the highest correlation occurs when the scarp is partitioned. The exponent and coefficient are largest for the

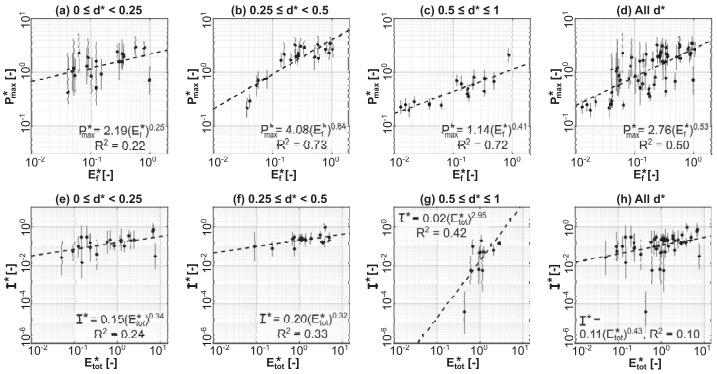

Figure 10. (a–d) Relationship between peak normalized energy flux (E^*_f, measured at Paros 1) and peak normalized impact pressure (P^*_{max}, measured at the scarp) for subsets of the data corresponding to various nondimensional depths d^*. (e–h) Relationship between total normalized wake energy (E^*_{tot}, measured at Paros 1) and normalized impulse (I^*, measured at the scarp). In all subplots, the points indicate the average of the measurements from each load cell during a given wake event, with error bars indicating the standard error of the mean.

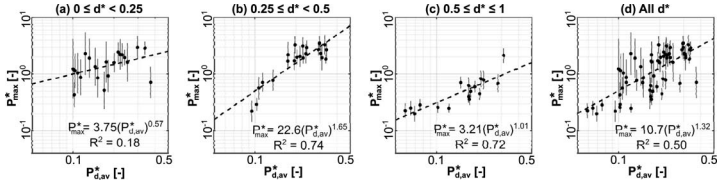

Figure 11. Relationship between normalized depth-averaged dynamic pressure ($P^*_{d,av}$, measured at Paros 1) and peak normalized impact pressure (P^*_{max}, measured at the scarp) for subsets of the data corresponding to various nondimensional depths d^*. In all subplots, the points indicate the average of the measurements from each load cell during a given wake event, with error bars indicating the standard error of the mean.

$0.25 < d^* < 0.5$ depth range, signifying the higher overall impact forces for a given wave condition.

Relationship between Total Energy and Impulse

Alternatively, it was possible to relate the nondimensional total energy at Paros 1, E^*_{tot}, which is given by Equation (5), to the nondimensional impulse on the scarp, I^*, which is given by Equation (12). This empirical model incorporates the energy of the entire wave train as opposed to just the maximum wave, and it evaluates if the total energy from a single vessel passage can be used as a meaningful metric to predict forces. As seen in Figure 10e–h, the relationship between these variables is generally poorer than that observed for the variables considered in the previous section. The best-fit relationships were:

$$I^* = 0.15\left(E^*_{tot}\right)^{0.34} \quad (0 \le d^* < 0.25)$$

$$I^* = 0.20\left(E^*_{tot}\right)^{0.32} \quad (0.25 \le d^* < 0.5)$$

$$I^* = 0.02\left(E^*_{tot}\right)^{2.95} \quad (0.5 \le d^* \le 1)$$

$$I^* = 0.11\left(E^*_{tot}\right)^{0.43} \quad (0 \le d^* \le 1) \qquad (15)$$

with R^2 values of 0.24, 0.33, 0.42, and 0.10, respectively (Figure 10e–h). The exponents and coefficients are similar for the lower scarp ($d^* < 0.5$), but the R^2 values are generally low. The highest correlation occurs when $0.5 \le d^* \le 1$, but the correlation is fairly poor compared to the regression analysis with maximum wave power; see Equation (14). This model as presented has much less explanatory power, and therefore impulse is not likely to be a meaningful metric with which to evaluate vessel impact forces.

Relationship between Peak Impact Pressure and Dynamic Pressure

The best-fit relationships between P^*_{max} and $P^*_{d,av}$ were:

$$P^*_{max} = 3.75\left(P^*_{d,av}\right)^{0.57} \quad (0 \le d^* < 0.25)$$

$$P^*_{max} = 22.59\left(P^*_{d,av}\right)^{1.65} \quad (0.25 \le d^* < 0.5)$$

$$P^*_{max} = 3.21\left(P^*_{d,av}\right)^{1.01} \quad (0.5 \le d^* \le 1)$$

$$P^*_{max} = 10.73\left(P^*_{d,av}\right)^{1.32} \quad (0 \le d^* \le 1) \qquad (16)$$

with R^2 values of 0.18, 0.74, 0.72, and 0.50, respectively (Figure 11). For low water depths ($d^* < 0.25$), the strength of the model fit is poor with greater uncertainty in the data. In contrast, the strength of the model fits for moderate to high water levels is generally good. However, for $d^* > 0.5$, the relationship is nearly linear as opposed to exponential. This is the regime where wave reflection is more prominent, and the forces are likely produced by the dynamic pressure of pulsating waves as opposed to the impulsive pressure from breaking waves.

DISCUSSION

A primary metric used in wave erosion studies is the wave energy flux, or wave power. As such, the load cell measurements are presented in terms of the wave energy flux and wave energy to determine the degree to which impact forces directly relate to vessel wake characteristics.

Impact Pressures

Of the roughly 100 wake events with a height exceeding the threshold of $H > 0.1$ m at Paros 1, peak energy fluxes were typically less than 200 W/m, with maximum values reaching 600 W/m. These values are very similar to average values estimated for wind waves within shallow lagoons (Mariotti and Fagherazzi, 2010; Schwimmer, 2001). Approximately 50% of impact pressures were less than 2 kPa, while the largest impact pressures approached or exceeded 10 kPa. Considering that wave impacts are the primary driver of edge erosion (directly *via* surface erosion, or indirectly *via* mass failure), it is instructive to compare impact pressures to critical shear stress and shear strength of marsh soils. For cohesive sediments, the critical stress for erosion ranges from <1 Pa to 6 Pa, depending on moisture content, degree of compaction, mineralogy, and other factors (Winterwerp and van Kesteren, 2004). The shear strength of marshes is considerably more variable. For example, based on >450 measurements across the Great Marsh in Massachusetts, Bloemendaal *et al*. (2021) found that shear strength within marsh banks ranged from 4 to 130 kPa with modal values in the range of 20–30 kPa. Note that the tensile strength of belowground biomass is necessarily incorporated into the measurements. Root tensile strength is an important consideration for macroscopic failures of a marsh scarp (Bendoni *et al*., 2014), but not necessarily surface erosion caused by wave impact (Feagin *et al*., 2009). Nonetheless, this study shows that the impact pressure from vessel wakes is many times greater than the critical erosion stress for cohesive sediments, and of the same order of magnitude as marsh shear

strength. Future work would benefit from incorporating shear strength and erosion measurements that are contemporaneous with the wave force measurements.

Relationship Between Energy Flux and Impact Pressure

Despite significant scatter, the data collected for this study suggest that nondimensional peak energy flux E_f^*, as given in Equation (3), which was derived from wave measurements approximately 5 m offshore of the scarp, may be used as an order-of-magnitude predictor of nondimensional peak impact pressure P_{max}^* on the marsh scarp following a power-law expression $P_{max}^* = \alpha\left(E_f^*\right)^{\beta}$. However, the parameters α and β, which define this relationship, may be site specific and/or dependent on tidal stage. Concerning the latter, this relationship was cast as a piecewise function due to the control of water level on wave breaking dynamics. The relatively smaller regression coefficients for the higher tide conditions are consistent with previous observations wherein larger impact forces occurred for $0.25 \leq d^* < 0.5$ (Figure 10).

Effect of Water Level on Pressure Distribution

Tidal stage is shown to exert strong control over the distribution of impact pressures, which are greatly reduced when mean water elevation is either near or below the toe of the scarp (dissipation by wave shoaling and early breaking) or when the marsh becomes submerged (dissipation by overtopping). When the water surface elevation is below the base of the scarp, and the tidal flat fronting the scarp is exposed, the incoming waves break before impinging upon the scarp, and the resulting force will be primarily due to runup as opposed to direct impact. As the water surface elevation increases, the waves begin to break on the scarp face, which results in higher impact pressures. As the water surface elevation increases further, the fronting tidal flat is mostly submerged, and there will be more instances of wave reflection as opposed to breaking. This produces a surge and reduces the impact pressure on the load cells. Once the scarp is fully submerged, the waves propagate into the marsh interior, further reducing the impact pressure on the scarp. Two videos illustrating this behavior are provided in the online Supplementary Information.

These field data agree with Kirkgöz (1995) and numerous other studies that showed peak pressures are distributed near the still-water level. Across the full tide range of the study site, peak pressures occurred when water levels were slightly below the midscarp elevation. However, the modeling results of Tonelli, Fagherazzi, and Petti (2010) showed that wave thrust (force per unit width) is maximum when water level approaches the marsh elevation, and then it rapidly decreases once the marsh is submerged. Wave thrust is calculated as the depth-integrated dynamic pressure of waves (Leonardi *et al*., 2016) and reaches a maximum beneath the wave crest. Since these are depth-integrated values, it is not surprising that maximum values are obtained for relative water depths approaching unity. However, this calculation method only describes the total load against the scarp and cannot distinguish between pulsating waves (slowly varying pressure) and impact waves resulting from wave breaking. This is an important consideration since impact pressures are at least 2.5× to 10× the nonbreaking dynamic pressure as found in this study and others (Cuomo, Tirnidelli, and Allsop, 2007; Rajasekaran, Sannasiraj, and Sundar, 2010). While larger waves should theoretically generate larger total forces owing to the greater transfer of momentum at the boundary, impact pressures are not strictly associated with wave height, as indicated in Figure 9f. For this study, the results showed that maximum wake heights were realized for relative water depths >0.5, yet the largest impact pressures were generated by smaller wake heights for relative water depths <0.5.

The literature has shown that wave shape during breaking greatly affects the magnitude of impact pressure (*e.g*., Oumeraci, Klammer, and Partenscky, 1993; Schmidt, Oumeraci, and Partenscky, 1992). Waves that tend to produce the largest impact pressures are those described as plunging breakers, where the shape of the approaching wave front is near vertical with little to no air trapped between the wave front and the structure it strikes. Schmidt, Oumeraci, and Partenscky (1992) classified these waves as type 2 or type 3 plunging breakers and noted that this type of breaking occurs when the breaking depth d_b is slightly larger than the depth at the scarp d_{scarp}:

$$d_{scarp} = 0.80 d_b \tag{17}$$

To first approximation, wave breaking occurs when water depth is approximately equal to wave height (Galvin, 1972). The depth at pressure sensor P1 was approximately 0.4 m at typical low tides and approximately 0.8 m at typical high tides, while the majority of vessel wake heights were smaller than 0.4 m, and the largest wakes occurred near high tide when the likelihood of overtopping was greatest. Consequently, the wave breaking conditions necessary to generate large impact pressures were relatively infrequent. This substantiates the observations that larger impact forces occur when the tide is relatively low and corroborates the laboratory experiments of Bendoni *et al*. (2014). Therefore, the variation of still-water depth with tidal stage exerts significant control on breaking distance and thus regulates breaking type. However, interacting factors such as wave reflection and incident wave angle complicate wake-scarp interactions, which may explain the additional lateral variability in impact pressures shown in Figure 9d,e. From the data, the likelihood of perfect wave breaking appears to be maximized for a modest slope (roughly 1:10 between pressure sensors P2 and P1) within relative water depths $d^* \approx 0.5$. The laboratory experiments of Galvin (1968) described an inshore parameter $\frac{H_b}{gmT_p^2} = 0.068$ for identifying the transition between plunging and surging breaker types. For a bed slope (bs) of 0.1, this transition occurs at $H_b = 0.4$ m for 2.5 second waves and at 0.6 m for 3 second waves, which are typical periods for vessel wakes.

Implications and Applicability

While Priestas *et al*. (2015) found that wave energy flux correlated slightly better with erosion rate than did wave thrust, the collated data set of Leonardi *et al*. (2016) reinforces the generally linear relationship between lateral erosion rate and total wave exposure. Within the models, there exists a critical wave threshold above which erosion will occur. For

example, the critical wave energy flux used in Mariotti and Fagherazzi (2010) was 3–15 W depending on the presence of vegetation. It can be argued that this critical threshold for erosion may be refined by evaluating the relationship between actual wave impact pressures and marsh resistance, since wave exposure alone does not necessarily initiate erosion. The wave climate (wind or vessel generated) can be measured directly or estimated through a variety of hindcasting or modeling approaches (Bendoni *et al*., 2014; Leonardi *et al*., 2016; Marani *et al*., 2011; Mariotti and Fagherazzi, 2010; Schwimmer, 2001). The calculated wave energy flux could then be used with Equation (14) to determine the range of impact pressures that should be compared with shear strength and sediment cohesion. It is nevertheless important to note, as discussed in McLoughlin *et al*. (2015), that model-derived estimates of wave energy flux (or other metrics) are sensitive to methodological differences in computation and averaging. For example, the results may be affected by the decision to exclude or retain measurements of E_f for water depths exceeding the marsh elevation.

Approaches to stabilize marsh shorelines and protect against wave impact include the concepts of eco- and geo-engineering practices (*e.g*., Silliman *et al*., 2019). Typically, these consist of structures placed or inserted at the base of the scarp for bank stabilization (*e.g*., geotextiles, rock sills, and wood pilings) or structures placed offshore to attenuate wave energy (*e.g*., natural or nature-based oyster reefs, nearshore mounds using dredged material, *etc*.). However, there remain numerous knowledge gaps on how to design living shorelines to balance ecological function with engineering efficacy (Morris *et al*., 2019). Additionally, the effective use of any engineered solution requires at least a cursory understanding of the assailing forces against which the structure is designed to protect. Knowledge and prediction of the magnitude and distribution of wave impact forces are envisioned to assist in the selection of the appropriate structure, the design process, and the estimation of life-cycle costs.

CONCLUSIONS

Marsh edge erosion is a complex process driven by mechanical energy transfer and the resisting characteristics of the base material. Previous studies have demonstrated that the rate of marsh retreat positively correlates with either wave power or dynamic wave pressure. This study presents a methodology to measure and predict impact pressures generated by shallow-draft vessels. Wave force measurements were collected using load cells—not previously applied to marsh settings—along an actively eroding section of the IWW in northeastern Florida.

Impact pressures from small-draft vessel wakes generally ranged from 1 to 10 kPa and were sensitive to tidal elevation. Maximum pressures occurred when the mean water level was just below the midpoint of the scarp, and impact pressures decayed as the mean depth either increased or decreased. Impact pressures at low relative water depths were reduced due to early wave breaking on the mud flat, whereas impact pressures were likewise reduced for relative water depths exceeding 0.5 because of increased instances of wave reflection and/or overtopping. Therefore, wave-breaking type and shape, which are dependent on slope and water depth, have more influence on the magnitude of impact pressures than does wave height alone.

Peak impact pressures can be predicted to order-of-magnitude values using the relations derived from wave power, $P^*_{max} = \alpha\left(E^*_f\right)^{\beta}$, or dynamic pressure, $P^*_{max} = \gamma\left(P^*_{d,av}\right)^{\delta}$, for depth-specific fitted parameters α, β, γ, and δ. These empirical relationships were partitioned into three segments to account for the pronounced effect of different water levels on impact pressures. Wave power and dynamic pressure both showed higher correlations with impact pressure for $0.25 \leq d^* < 1$, yet in both cases, the greatest impacts were predicted to occur for water levels in the middle portion of the tidal frame ($0.25 \leq d^* < 0.5$).

The sensitivity of impact force to tidal stage suggests that wave energetics (breaking *vs*. reflection) and scarp morphology (ramp *vs*. near-vertical surface) combine to produce a force pattern that favors maximum impact below the scarp midpoint and that is independent of the offshore wake characteristics for shallow-draft vessels. While more data are needed to further refine the relationship between impact forces and vessel wake characteristics, this paper presented new information for the measurement and prediction of wave impact forces, which can be used to elucidate further the complex dynamics of marsh edge erosion, particularly in regions dominated by shallow-draft vessel operations.

ACKNOWLEDGMENTS

This work was supported by the Navigation Systems Research Program and the Coastal Inlets Research Program of the U.S. Army Corps of Engineers. The authors would like to thank the following for their assistance in the field: John Bull, De'Arius Christmas, John Gaskin, Cody Johnson, and Michael Ramirez. We also extend our thanks to the staff of the University of Florida Whitney Laboratory for Marine Bioscience for providing lodging and logistical support during the field study. Dr. Alex Kolker and the Louisiana Universities Marine Consortium provided assistance for early field tests, for which we are grateful. We appreciate Dr. Chris Makowski, Journal of Coastal Research editor-in-chief, for timely editorial support, and the two anonymous reviewers for their helpful suggestions and comments that improved the manuscript.

LITERATURE CITED

Allen, J.R.L., 1989. Evolution of salt-marsh cliffs in muddy and sandy systems: A qualitative comparison of British west-coast estuaries. *Earth Surface Processes and Landforms*, 14(1), 85–92. doi:10.1002/esp.3290140108

Allen, J.R.L., 2000. Morphodynamics of Holocene salt marshes: A review sketch from the Atlantic and southern North Sea coasts of Europe. *Quaternary Science Reviews*, 19(12), 1155–1231. doi:10.1016/S0277-3791(99)00034-7

Bendoni, M.; Francalanci, S.; Cappietti, L., and Solari, L., 2014. On salt marshes retreat: Experiments and modeling toppling failures induced by wind waves. *Journal of Geophysical Research: Earth Surface*, 119(3), 603–620. doi:10.1002/2013JF002967

Bendoni, M.; Georgiou, I.; Roelvink, D., and Oumeraci, H., 2019. Numerical modelling of the erosion of marsh boundaries due to wave impact. *Coastal Engineering*, 152(103514). doi:10.1016/j.coastaleng.2019.103514

Bilkovic, D.; Mitchell, M.; Davis, H.J.; Andrews, E.; King, A.; Mason, P.; Tahvildari, N.; Davis, J., and Dixon, R.L., 2019. Defining boat wake impacts on shoreline stability toward management and policy solutions. *Ocean and Coastal Management*, 182(104945). doi:10.1016/j.ocecoaman.2019.104945

Bilkovic, D.; Mitchell, M.; Davis, J.; Andrews, E.; King, A.; Mason, P.; Herman, J.; Tahvildari, N., and Davis, J., 2017. *Review of Boat Wake Wave Impacts on Shoreline Erosion and Potential Solutions for the Chesapeake Bay*. Edgewater, Maryland: Scientific and Technical Advisory Committee to the Chesapeake Bay Program, *STAC Publication 17-002*, 68p.

Bloemendaal, L.J.H.; FitzGerald, D.M.; Hughes, Z.J.; Novak, A.B., and Phippen, P., 2021. What controls marsh edge erosion? *Geomorphology*, 386(107745). doi:10.1016/j.geomorph.2021.107745

Bridges, T.S.; Wagner, P.W.; Burks-Copes, K.A.; Bates, M.E.; Collier, Z.A.; Fischenich, C.J.; Gailani, J.Z.; Leuck, L.D.; Piercy, C.D.; Rosati, J.D.; Russo, E.J.; Shafer, D.J.; Suedel, B.C.; Vuxton, E.A., and Wamsley, T.V., 2015. *Use of Natural and Nature-Based Features (NNBF) for Coastal Resilience*. Vicksburg, Mississippi: U.S. Army Corps of Engineers, *Special Report SR-15-1*, 477p.

Buckingham, C.A.; Lefebvre, L.W.; Schaefer, J.M., and Kochman, H.I., 1999. Manatee response to boating activity in a thermal refuge. *Wildlife Society Bulletin*, 27(2), 514–522. www.jstor.org/stable/3783921

Burgin, S. and Hardiman, N., 2011. The direct physical, chemical and biotic impacts on Australian coastal waters due to recreational boating. *Biodiversity and Conservation*, 20(4), 683–701. doi:10.1007/s10531-011-0003-6

Carreño, A. and Lloret, J., 2021. Environmental impacts of increasing leisure boating activity in Mediterranean coastal waters. *Ocean and Coastal Management*, 209(105693). doi:10.1016/j.ocecoaman.2021.105693

Cuomo, G.; Tirnidelli, M., and Allsop, W., 2007. Wave-in-deck loads on exposed jetties. *Coastal Engineering*, 54(9), 657–679. doi:10.1016/j.coastaleng.2007.01.010

Fagherazzi, S.; Mariotti, G.; Leonardi, N.; Canestrelli, A.; Nardin, W., and Kearney, W.S., 2019. Salt marsh dynamics in a period of accelerated sea-level rise. *Journal of Geophysical Research: Earth Surface*, 125(8), e2019JF005200. doi:10.1029/2019JF005200

Feagin, R.A.; Lozada-Bernard, S.M.; Ravens, T.M.; Möller, I.; Yeager, K.M., and Baird, A.H., 2009. Does vegetation prevent wave erosion of salt marsh edges? *Proceedings of the National Academy of Sciences of the United States of America*, 106(25), 10109–10113. doi:10.1073/pnas.0901297106

Finotello, A.; Marani, M.; Carniello, L.; Pivato, M.; Roner, M.; Tommasini, L., and D'Alpaos, A., 2020. Control of wind-wave power on morphological shape of salt marsh margins. *Water Science and Engineering*, 13(1), 45–56. doi:10.1016/j.wse.2020.03.006

Gallivan, L.B. and Davis, R.A., Jr., 1981. Sediment transport in a microtidal estuary: Matanzas River, Florida (USA). *Marine Geology*, 40(1–2), 69–83. doi:10.1016/0025-3227(81)90043-8

Galvin, C.J., Jr., 1968. Breaker type classification on three laboratory beaches. *Journal of Geophysical Research*, 73(12), 3651–3659. doi:10.1029/jb073i012p03651

Galvin, C.J., Jr., 1972. Wave breaking in shallow water. *In:* Meyer, R.E. (ed.), *Waves on Beaches and Resulting Sediment Transport*. New York: Academic Press, pp. 413–456.

Herbich, J.B. and Schiller, R.E., Jr., 1985. Surges and waves generated by ships in a constricted channel. *In:* Edge, B.L. (ed.), *Coastal Engineering 1984*. Houston, Texas: American Society of Civil Engineers, pp. 3212–3226. doi:10.1061/9780872624382

Houser, C., 2010. Relative importance of vessel-generated and wind waves to salt marsh erosion in a restricted fetch environment. *Journal of Coastal Research*, 26(2), 230–240. doi:10.2112/08-1084.1

Hughes, S.A., 2004a. Estimation of wave run-up on smooth, impermeable slopes using the wave momentum flux parameter. *Coastal Engineering*, 51(11–12), 1085–1104. doi:10.1016/j.coastaleng.2004.07.025

Hughes, S.A., 2004b. Wave momentum flux parameter: A descriptor for nearshore waves. *Coastal Engineering*, 51(11–12), 1067–1084. doi:10.1016/j.coastaleng.2004.07.026

Karimpour, A., 2020. *OCEANLYZ User Manual, Release 1.5*. oceanlyz.readthedocs.io

Karimpour, A. and Chen, Q., 2017. Wind wave analysis in depth limited water using OCEANLYZ, a MATLAB toolbox. *Computers and Geosciences*, 106, 181–189. doi:10.1016/j.cageo.2017.06.010

Kirkgöz, M.S., 1995. Breaking wave impact on vertical and sloping coastal structures. *Ocean Engineering*, 2(1), 35–48. doi:10.1016/0029-8018(93)E0006-E

Leonardi, N.; Defne, Z.; Ganju, N., and Fagherazzi, S., 2016. Salt marsh erosion rates and boundary features in a shallow bay. *Journal of Geophysical Research: Earth Surface*, 121(10), 1861–1875. doi:10.1002/2016JF003975

Marani, M.; D'Alpaos, A.; Lanzoni, S., and Santalucia, M., 2011. Understanding and predicting wave edge erosion of marsh edges. *Geophysical Research Letters*, 38(L21401), 1–5. doi:10.1029/2011GL048995

Mariotti, G. and Carr, J., 2014. Dual role of salt marsh retreat: Long-term loss and short-term resilience. *Water Resources Research*, 50(4), 2963–2974. doi:10.1002/2013WR014676

Mariotti, G. and Fagherazzi, S., 2010. A numerical model for the coupled long-term evolution of salt marshes and tidal flats. *Journal of Geophysical Research: Earth Surface*, 115(F1), 1–15. doi:10.1029/2009JF001326

Mariotti, G. and Fagherazzi, S., 2020. Critical width of tidal flats triggers marsh collapse in the absence of sea-level rise. *Proceedings of the Academy of Sciences of the United States of America*, 110(14), 5353–5356. doi:10.1073/pnas.1219600110

Maynord, S.T., 2003. *Ship Effects Before and After Deepening of Sabine-Neches Waterway, Port Arthur, Texas*. Vicksburg, Mississippi: U.S. Army Corps of Engineers, *Technical Report TR-03-15*, 85p.

Maynord, S.T., 2005. Wave height from planing and semi-planing small boats. *River Research and Applications*, 21(1), 1–17. doi:10.1002/rra.803

Maynord, S.T., 2007. *Ship Forces on the Shoreline of the Savannah Harbor Project*. Vicksburg, Mississippi: U.S. Army Corps of Engineers, *Technical Report TR-07-7*, 149p.

McLoughlin, S.M.; Wiberg, P.L.; Safak, I., and McGlathery, K.J., 2015. Rates and forcing of marsh edge erosion in a shallow coastal bay. *Estuaries and Coasts*, 38(2), 620–638. doi:10.1007/s12237-014-9841-2

Morris, R.L.; Bilkovic, D.M.; Boswell, M.K.; Bushek, D.; Cebrian, J.; Goff, J.; Kibler, K.M.; La Peyre, M.K.; McClenachan, G.; Moody, J.; Sacks, P.; Shinn, J.P.; Sparks, E.L.; Temple, N.A.; Walters, L.J.; Webb, B.M., and Swearer, S.E., 2019. The application of oyster reefs in shoreline protection: Are we over-engineering for an ecosystem engineer? *Journal of Applied Ecology*, 56(7), 1703–1711. doi:10.1111/1365-2664.13390

Oumeraci, H.; Klammer, P., and Partenscky, H.W., 1993. Classification of breaking wave loads on vertical structures. *Journal of Waterways, Port, Coastal and Ocean Engineering*, 119(4), 381–397. doi:10.1061/(ASCE)0733-950X(1993)119:4(381)

Priestas, A.M.; Mariotti, G.; Leonardi, N., and Fagherazzi, S., 2015. Coupled wave energy and erosion dynamics along a salt marsh boundary, Hog Island Bay, Virginia, USA. *Journal of Marine Science and Engineering*, 3(3), 1041–1065. doi:10.3390/jmse3031041

Rajasekaran, C.; Sannasiraj, S., and Sundar, V., 2010. Breaking wave impact pressure on a vertical wall. *International Journal of Ocean and Climate Systems*, 1(3–4), 155–166. doi:10.1260/1759-3131.1.3-4.155

Rapaglia, J.; Zaggia, L.; Ricklefs, K.; Gelinas, M., and Bokuniewicz, H., 2011. Characteristics of ships' depression waves and associated sediment resuspension in Venice Lagoon, Italy. *Journal of Marine Systems*, 85(1–2), 45–56. doi:10.1016/j.jmarsys.2010.11.005

Safak, I.; Angelini, C., and Sheremet, A., 2021. Boat wake effects on sediment transport in intertidal waterways. *Continental Shelf Research*, 222,(04422. doi:10.1016/j.csr.2021.104422

Safak, I.; Norby, P.L.; Dix, N.; Grizzle, R.E.; Southwell, M.; Veenstra, J.J.; Acevedo, A.; Cooper-Kolb, T.; Massey, L.; Sheremet, A., and Angelini, C., 2020. Coupling breakwalls with oyster restoration structures enhances living shoreline performance along energetic

shorelines. *Ecological Engineering*, 158, 106071. doi:10.1016/j.ecoleng.2020.106071

Schmidt, R.; Oumeraci, H., and Partenscky, H.W., 1992. Impact loads induced by plunging breakers on vertical structures. *In:* Edge, B.L. (ed.), *Coastal Engineering 1992*. Venice, Italy: American Society of Civil Engineers, pp. 1545–1558. doi:10.1061/9780872629332

Schwimmer, R.A., 2001. Rates and processes of marsh shoreline erosion in Rehoboth Bay, Delaware, USA. *Journal of Coastal Research*, 17(3), 672–683. doi:10.2307/4300218

Shuster, R.; Sherman, D.J.; Lorang, M.S.; Ellis, J.T., and Hopf, F., 2020. Erosive potential of recreational boat wakes. *In:* Malvárez, G. and Navas, F. (eds.), *Global Coastal Issues of 2020*. *Journal of Coastal Research*, Special Issue No. 95, pp. 1279–1283. doi:10.2112/SI95-247.1

Silliman, B.R.; He, Q.; Angelini, C.; Smith, C.S.; Kirwan, M.L.; Daleo, P.; Renzi, J.J.; Butler, J.; Osborne, T.Z.; Nifong, J.C., and van de Koppel, J., 2019. Field experiments and meta-analysis reveal wetland vegetation as a crucial element in the coastal protection paradigm. *Current Biology*, 29(11), 1800–1806. doi:10.1016/j.cub.2019.05.017

Styles, R. and Hartman, M.A., 2019. Effect of tidal stage on sediment concentrations and turbulence by vessel wake in a coastal plain saltmarsh. *Journal of Marine Science and Engineering*, 7(6), 192. doi:10.3390/jmse7060192

Tonelli, M.; Fagherazzi, S., and Petti, M., 2010. Modeling wave impact on salt marsh boundaries. *Journal of Geophysical Research: Oceans*, 115(C09028), 1–17. doi:10.1029/2009JC006026

Valentine, K. and Mariotti, G., 2019. Wind-driven water level fluctuations drive marsh edge erosion variability in microtidal coastal bays. *Continental Shelf Research*, 176, 76–89. doi:10.1016/j.csr.2019.03.002

van de Koppel, J.; van der Wal, D.; Bakker, J.P., and Herman, P.M., 2005. Self-organization and vegetation collapse in salt marsh ecosystems. *American Naturalist*, 165(1), E1–E12. doi:10.1086/426602

Van der Wal, D.; Wielemaker-Van den Dool, A., and Herman, P.M.J., 2008. Spatial patterns, rates and mechanisms of saltmarsh cycles (Westerschelde, The Netherlands). *Estuarine and Coastal Shelf Science*, 76(2), 375–368. doi:10.1016/j.ecss.2007.07.017

Winterwerp, J.C. and van Kesteren, W.G.M., 2004. *Introduction to the Physics of Cohesive Sediment Dynamics in the Marine Environment*, 1st edition. New York: Elsevier Science, 576p.